K. Mahesh
Aerospace Engineering and Mechanics,
University of Minnesota,
107 Akerman Hall,
Minneapolis, MN 55455

G. Constantinescu
Civil and Environmental Engineering,
University of Iowa,
Iowa City, IA 52242

S. Apte

G. Iaccarino

F. Ham

P. Moin

Center for Integrated Turbulence Simulations,
Stanford University,
Building 500,
Stanford, CA 94305

Large-Eddy Simulation of Reacting Turbulent Flows in Complex Geometries

*Large-eddy simulation (LES) has traditionally been restricted to fairly simple geometries. This paper discusses LES of reacting flows in geometries as complex as commercial gas turbine engine combustors. The incompressible algorithm developed by Mahesh et al. (J. Comput. Phys., 2004, **197**, 215–240) is extended to the zero Mach number equations with heat release. Chemical reactions are modeled using the flamelet/progress variable approach of Pierce and Moin (J. Fluid Mech., 2004, **504**, 73–97). The simulations are validated against experiment for methane-air combustion in a coaxial geometry, and jet-A surrogate/air combustion in a gas-turbine combustor geometry.*
[DOI: 10.1115/1.2179098]

1 Introduction

Large-eddy simulation (LES) is a three-dimensional, unsteady, computational approach where the unsteady Navier-Stokes equations are spatially filtered, the large scales are directly computed, and the effect of the filtered scales on the resolved scales is modeled. LES is considered very attractive for predicting scalar mixing and pollutant formation [1–6] in turbulent reacting flows. Presently, LES and direct numerical simulation (DNS) have largely been used to study turbulent flows in simple configurations. Figure 1 contrasts an axisymmetric coaxial combustor to a commercial gas-turbine engine combustor. The considerable increase in geometrical complexity is apparent. The focus of this paper is development of the capability to reliably perform LES of reacting flows in geometries as complex as commercial gas-turbine combustors.

Key elements of this capability include subgrid models for turbulent reacting flows, and the numerical methods used to solve the resulting equations. Peters [7] provides a detailed review of modeling approaches to turbulent combustion. Some of the key approaches are flamelets [8], conditional moment closure [9], probability density function [10], and linear-eddy modeling [11]. Most of these ideas were originally proposed in the Reynolds-averaged (RANS) context, and recently have been extended to the LES framework (e.g., [12–19,2]). Different approaches to subgrid modeling exist; this paper uses the flamelet/progress-variable approach of Pierce and Moin [2].

The numerical method used to solve the LES equations is quite important, since numerical errors tend to be largest at the smallest resolved scales, which is also where the subgrid model is most active. Numerical errors can, therefore, compete with, and even overwhelm the effect of the subgrid model. Dissipative errors are considered more harmful than dispersive errors in this regard (e.g., [20]). However, the complete absence of numerical dissipation can result in nonlinear instability at coarse resolutions. For incompressible flows, one solution to this problem is to constrain the numerical scheme to discretely conserve not only mass and momentum, but also kinetic energy. This approach has proved quite successful on structured grids (e.g., [21–24]). Extension to unstructured grids were performed by Mahesh et al. [1], who validate their approach for flows ranging from the Taylor problem to incompressible flow in a commercial gas-turbine combustor. This paper extends [1] approach for constant density incompressible flows to zero Mach number reacting flows.

The paper is organized as follows. Section 2 discusses discrete energy conservation, and summarizes the algorithm developed by Mahesh et al. [1] for constant density incompressible flows. The incompressible algorithm is extended to variable density flow with heat release, and combined with the flamelet/progress-variable subgrid model of [2] in Sec. 3. Validation results for reacting flow in a coaxial and gas turbine combustor are discussed in Secs. 3.4 and 3.5, respectively.

2 Constant Density Incompressible Flow

The incompressible Navier-Stokes and continuity equations are

$$\frac{\partial u_i}{\partial t}+\frac{\partial u_i u_j}{\partial x_j}=-\frac{\partial p}{\partial x_i}+\nu\frac{\partial^2 u_i}{\partial x_j \partial x_j};\quad \frac{\partial u_i}{\partial x_i}=0, \tag{1}$$

where u_i, p, and ν denote the velocity, pressure, and kinematic viscosity, respectively. Note that density is absorbed into the pressure. Spatial filtering (denoted by the overbar) with a commutative filter yields the incompressible LES equations:

$$\frac{\partial \bar{u}_i}{\partial t}+\frac{\partial \bar{u}_i \bar{u}_j}{\partial x_j}=-\frac{\partial \bar{p}}{\partial x_i}+\nu\frac{\partial^2 \bar{u}_i}{\partial x_j x_j}+\frac{\partial \tau_{ij}}{\partial x_j};\quad \frac{\partial \bar{u}_i}{\partial x_i}=0. \tag{2}$$

Contributed by the Applied Mechanics Division of ASME for publication in the JOURNAL OF APPLIED MECHANICS. Manuscript received December 15, 2003; final manuscript received November 9, 2005. Review conducted by D. Siginer. Discussion on the paper should be addressed to the Editor, Prof. Robert M. McMeeking, Journal of Applied Mechanics, Department of Mechanical and Environmental Engineering, University of California–Santa Barbara, Santa Barbara, CA 93106-5070, and will be accepted until four months after final publication in the paper itself in the ASME JOURNAL OF APPLIED MECHANICS.

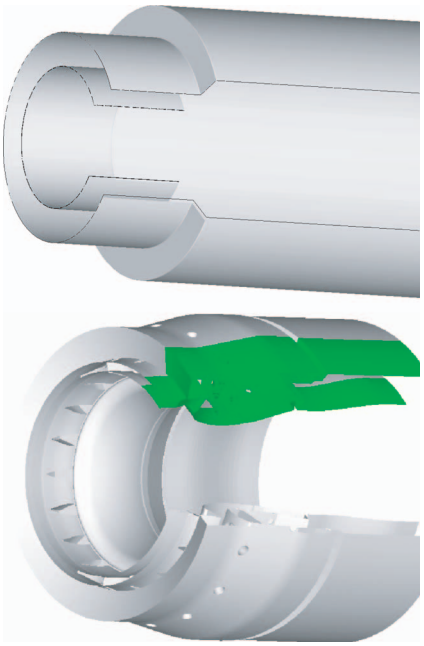

Fig. 1 Contrast between an idealized coaxial dump combustor (*a*), and the combustor from a Pratt and Whitney gas-turbine engine (*b*)

where $\tau_{ij}=\overline{u_iu_j}-\bar{u}_i\bar{u}_j$ is the subgrid stress, and is modeled. The dynamic Smagorinsky model [25] was used to obtain τ_{ij} in all simulations reported in this paper. The Smagorinsky model assumes that $q_{ij}=-2C\Delta^2|\bar{S}|\bar{S}_{ij}$, where q_{ij} denotes the anisotropic part of the subgrid stress, Δ denotes the grid-filter width, and $\bar{S}_{ij}$ denotes the filtered strain-rate tensor. The least-squares approach [26] yields $C\Delta^2=-\frac{1}{2}(L_{ij}M_{ij}/M_{kl}M_{kl})$, where $L_{ij}=\widehat{\bar{u}_i\bar{u}_j}-\hat{\bar{u}}_i\hat{\bar{u}}_j$, and $M_{ij}=(\hat{\Delta}/\Delta)^2|\hat{\bar{S}}|\hat{\bar{S}}_{ij}-|\widehat{\bar{S}}|\widehat{\bar{S}}_{ij}$. The test-filter (denoted by $\hat{}$) is a top-hat filter that uses information from neighboring volumes. The filter width is defined as $V^{1/3}$ where V denotes the element volume, and the ratio of filter widths $(\hat{\Delta}/\Delta)$ is 2.

A numerical method that emphasizes discrete energy conservation was developed for the above equations on unstructured grids with hybrid, arbitrary elements. The algorithm is described in detail by Mahesh [1] and will only be summarized here. For incompressible flows, discrete energy conservation refers to the fact that the convective and pressure terms in the discrete kinetic energy equation are expressible in divergence form. In the absence of viscosity, the continuity and momentum equations imply that

$$\frac{\partial}{\partial t}\frac{u_iu_i}{2}+\frac{\partial}{\partial x_j}\frac{u_iu_iu_j}{2}=-\frac{\partial}{\partial x_i}pu_i. \tag{3}$$

Using Gauss' theorem, the above equation implies that the integral of the kinetic energy over the computational domain is determined by its boundary fluxes and pressure-work at the boundaries. This is a useful property for a numerical algorithm since it implies that the sum of positive quantities is bounded. However, unlike the continuous equations, mass and momentum conservation do not imply kinetic energy conservation for the discrete equations; this constraint has to be imposed.

Mahesh et al. [1] method is a predictor-corrector formulation that emphasizes energy conservation for the convection and pressure terms on arbitrary grids. The cell velocities u_i and the face-normal velocities v_n are treated as essentially independent variables. Time advancement may be explicit using the second-order Adams-Bashforth method, or fully implicit using the Crank-Nicholson scheme along with linearization of the nonlinear terms. The nonlinear and viscous terms are used to obtain a predictor value for the cell-centered velocities. The predicted values of u_i are used to obtain predicted values for the face-normal velocities, which are then projected to obtain the pressure, p. Once p is obtained, the Cartesian velocities are updated as

$$\frac{u_i^{k+1}-\hat{u}_i}{\Delta t}=-\frac{\partial p}{\partial x_i}. \tag{4}$$

The discrete expression used for $\partial p/\partial x_i$ affects the robustness of the solution on highly skewed grids. A least-squares expression that alleviates this problem was, therefore, derived for the pressure gradient term in Eq. (4). Section 3 extends the incompressible algorithm to the zero Mach number variable density equations.

2.1 Constant Density Flow in a Coaxial Combustor. The coaxial combustor (Fig. 1) is a model problem that has some of the key physical features of gas-turbine combustors. Detailed experimental data [27] are available, which make it an ideal test problem. Figure 1 shows a cross section of the axially symmetric geometry. The flow involves interaction between two streams: Fully developed turbulent pipe flow, and turbulent, annular swirling flow. Both streams discharge into an expansion. The resulting axial adverse pressure gradient causes the flow to diverge radially, and sets up a recirculation region in the expansion. If the two streams were reacting, this recirculation region would help stabilize the flame.

LES was performed under conditions corresponding to Sommerfeld and Qiu's [27] (1991) experiments in a coaxial combustor geometry. The primary jet has a radius of 16 mm and the secondary annular jet extends over the radial interval of 19–32 mm. The outer radius of the annulus is 32 mm, and the test section is 960 mm long. The test section connects to a stagnation chamber of length 640 mm and radius 288 mm. The Reynolds number of the primary jet is 26,200 and the swirl number (ratio of mean azimuthal to axial momentum) in the annulus is 0.47. The ratio of flow rates of the annular jet to the primary jet is 3.87. Sommerfeld and Qiu's [27] experiments had glass beads in the primary jet. The present algorithm was extended to account for particles using a Lagrangian approach, and LES including the particles was performed by Apte et al., [28,29]. Here, we only consider the gas phase.

An unstructured grid of 1.6×10^6 hexahedral volumes was generated, with approximately 0.9×10^6 elements in the first half of the test section. The smallest grid spacing was approximately 32 μm near the walls, and in the shear layers close to the annular inlet into the test section. Unsteady velocities corresponding to turbulent pipe flow, and turbulent annular swirling flow, from a separate computation were specified at the inflow. Convective boundary conditions were imposed at the outflow. Profiles at six stations of mean streamwise, radial and azimuthal velocities and turbulence kinetic energy are compared to experiment in Fig. 2, and good agreement is observed.

3 Reacting Flow

3.1 Governing Equations. The incompressible algorithm is extended to turbulent reacting flows. The zero Mach number equations are used to represent the gas-phase, and the flamelet/progress variable approach of Pierce and Moin [2] is used to model the effect of chemical reactions. The governing equations in the absence of spatial filtering are:

$$\frac{\partial\rho u_i}{\partial t}+\frac{\partial\rho u_iu_j}{\partial x_j}=-\frac{\partial p}{\partial x_i}+\frac{\partial}{\partial x_j}\left[\mu\left(\frac{\partial u_i}{\partial x_j}+\frac{\partial u_j}{\partial x_i}-\frac{2}{3}\frac{\partial u_k}{\partial x_k}\delta_{ij}\right)\right], \tag{5a}$$

$$\frac{\partial\rho u_i}{\partial x_i}=-\frac{\partial\rho}{\partial t}, \tag{5b}$$

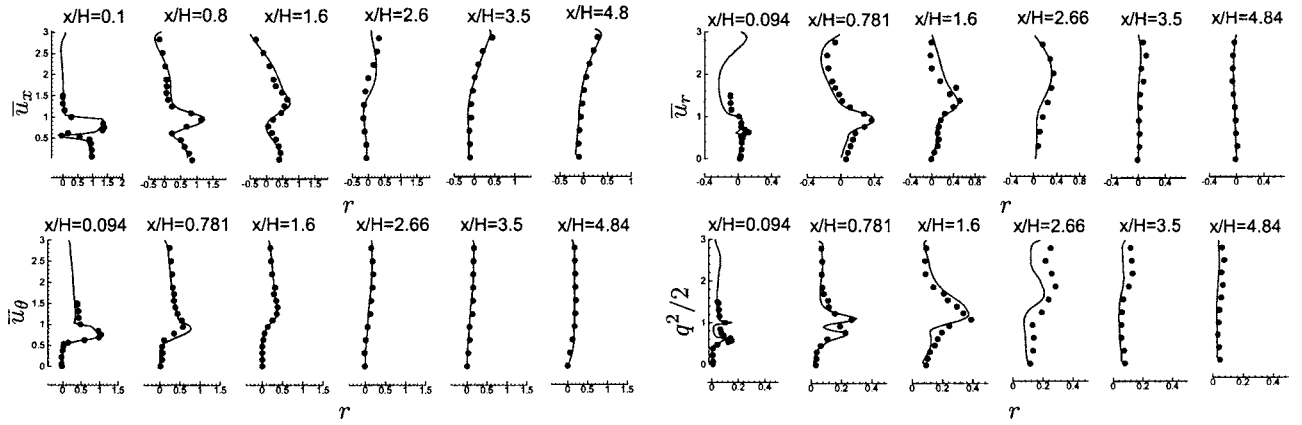

Fig. 2 Profiles of mean velocity and turbulent kinetic energy in LES of incompressible swirling flow in a coaxial combustor geometry. The solid lines are LES results, and the symbols are data from experiments by Sommerfeld and Qiu [27]. *H* denotes the outer radius of the annular section, $\bar{u}_x$, $\bar{u}_r$, and $\bar{u}_\theta$ denote the mean axial, radial, and azimuthal velocity, respectively, and $q^2/2$ denotes the turbulent kinetic energy.

$$\frac{\partial \rho Z}{\partial t} + \frac{\partial}{\partial x_j}\rho Z u_j = \frac{\partial}{\partial x_i}\left(\rho\alpha\frac{\partial Z}{\partial x_i}\right), \tag{5c}$$

$$\frac{\partial \rho C}{\partial t} + \frac{\partial}{\partial x_j}\rho C u_j = \frac{\partial}{\partial x_i}\left(\rho\alpha\frac{\partial C}{\partial x_i}\right) + \rho w_C. \tag{5d}$$

Here, Z denotes the mixture fraction which is a conserved scalar, and C is a progress variable that models the "progress" of the reaction. μ, α, and w_C denote the molecular viscosity, molecular scalar diffusivity and chemical source term, respectively.

The density, temperature, molecular viscosity, molecular diffusivity, reaction source terms in the progress variable equations, and chemical species are related to the mixture fraction and the progress variable through a flamelet library that is precalculated, given the specific fuel reactions, and the flow conditions in the combustor. The progress variable is chosen to represent overall flame behavior, and varies monotonically with the flame state. The single-parameter flamelet library is developed using stationary solutions to the one-dimensional reaction-diffusion equations. The unstable and the lower branches of the S-shaped curve are included so that the complete range of flame states, from completely extinguished (mixing without reaction) to completely reacted (equilibrium chemistry), is represented in the library. Arbitrarily complex chemical kinetic mechanisms as well as differential-diffusion effects can be included. The result is a complete set of flame states, in terms of mixture fraction and a single flamelet parameter denoted by λ (typically the scalar dissipation rate):

$$y_k = y_k(Z,\lambda), \quad T = T(Z,\lambda), \quad \rho = \rho(Z,\lambda), \quad \text{and} \quad w_k = w_k(Z,\lambda). \tag{6}$$

Here, y_k denotes the mass fractions of the chemical species, and T is the temperature.

3.2 Numerical Method. The Cartesian components of momentum, density and pressure are stored at the centroids of the computational elements, and the face-normal velocity is stored at the centroids of the faces. Note that once density is obtained from the flamelet library, the continuity equation can be imposed as a constraint on the momentum field, with the time-derivative of density as a source term. This constraint is enforced by the pressure, in a manner analogous to the enforcement of the incompressibility constraint for constant density flows. The computational approach is to first advance the mixture fraction, Z and the progress-variable C. The flamelet library yields the density, whose time-derivative is then computed. The cell-centered momentum is predicted using the convective, viscous, and pressure-gradient at the present time step. The predicted value of the momentum is then projected such that the continuity equation is satisfied. The projection step yields the pressure, whose gradient is computed using the same least-squares approximation as the incompressible algorithm [1], and is used to correct the cell-centered momentum

Details of the spatial discretization are provided below. Time advancement may be explicit (second-order Adams-Bashforth) or fully implicit (Crank-Nicholson). Using the notation $AB2/CN$ to denote use of the Adams-Bashforth or Crank-Nicholson operators, the predictor step for the momentum equation is given by

$$V\frac{\widehat{\rho u_i} - \rho u_i^n}{\Delta t} = AB2/CN(RHS_i) \tag{7}$$

where V denotes the volume of the computational element, Δt denotes the timestep, and

$$RHS_i = -\sum_{\text{faces of } cv} \rho u_i|_f v_N A_f + \sum_{\text{faces of } cv} \mu_f\left[\left(\left.\frac{\partial u_i}{\partial x_j}\right|_f + \left.\frac{\partial u_j}{\partial x_i}\right|_f\right) \times N_j A_f - \frac{2}{3}\left.\frac{\partial u_k}{\partial x_k}\right|_f N_i A_f\right] \tag{8}$$

where N_i denotes the outward normal at each face, the subscript, "f" denotes values computed at the faces, and the summation is over all faces of the control volume. Also, $\rho u_i|_f = (\rho u_i|_{icv1} + \rho u_i|_{icv2})/2$ where the subscripts, "$icv1$" and "$icv2$" denote the control volumes on either side of the face. The velocity gradient at the faces,

$$\left.\frac{\partial u_j}{\partial x_i}\right|_f = \frac{1}{2}\left(\left.\frac{\partial u_j}{\partial x_i}\right|_{icv1} + \left.\frac{\partial u_j}{\partial x_i}\right|_{icv2}\right)$$

where the gradient at the cell centers is computed using a least-squares formulation. Also,

$$\left.\frac{\partial u_i}{\partial x_j}\right|_f N_j = \frac{\partial u_i}{\partial N} = \frac{u_i^{icv2} - u_i^{icv1}}{d_f}.$$

The velocity divergence, $(\partial u_k/\partial x_k)|_f$ is computed by averaging its values at the neighboring cells, which are computed as

$$\frac{1}{V}\sum_{\text{faces of } cv} v_N A_f.$$

Once $\widehat{\rho u_i}$ is obtained at the cell centers, it is averaged to yield its value at the faces, $\widehat{\rho u_i}|_f$. Contraction with the face-normal vector yields $\rho\hat{v}_N$, which is corrected using

$$\frac{\rho v_N^{n+1} - \widehat{\rho v_N}}{\Delta t} = -\left.\frac{\partial \phi}{\partial N}\right|_f = -\frac{\phi_{icv2} - \phi_{icv1}}{d_f} \tag{9}$$

The continuity equation implies that $\Sigma_{\text{faces of } cv} \rho v_N A_f = -V(\partial\rho/\partial t)|_{cv}$. Here, ϕ denotes the corrected pressure, and d_f is the distance between the neighboring cells projected normal to the face. Invoking the continuity equation yields the following equation for ϕ

$$\Delta t \sum_{\text{faces of } cv} \frac{\phi_{nbr} - \phi_{cv}}{d_f} A_f = \sum_{\text{faces of } cv} \widehat{\rho v_N} A_f + V \left.\frac{\partial \rho}{\partial t}\right|_{cv}. \tag{10}$$

A multigrid approach is used to solve the above equation for the corrected pressure. Once ϕ is obtained, Eq. (9) is used to obtain ρv_N^{n+1}. The momentum at the cell centers is obtained using

$$\rho u_i - \widehat{\rho u_i} = -\Delta t \frac{\partial \phi}{\partial x_i}. \tag{11}$$

The least-squares formulation used by Mahesh et al. [1] is used to compute the pressure gradient in the above correction step and update ρu_i.

3.3 LES Model. The LES model is that proposed by Pierce and Moin [2]. Favre filtering of the governing equations (5*a*)–(5*d*) (denoted by $\tilde{}$, $\tilde{f} = \overline{\rho f}/\bar{\rho}$) yields the LES equations.

$$\frac{\partial \bar{\rho}\tilde{u}_i}{\partial t} + \frac{\partial \bar{\rho}\tilde{u}_i\tilde{u}_j}{\partial x_j} = -\frac{\partial \bar{p}}{\partial x_i} + \frac{\partial}{\partial x_j}\left[\bar{\mu}\left(\frac{\partial \tilde{u}_i}{\partial x_j} + \frac{\partial \tilde{u}_j}{\partial x_i} - \frac{2}{3}\frac{\partial \tilde{u}_k}{\partial x_k}\delta_{ij}\right)\right] + \frac{\partial \tau_{ij}}{\partial x_j}, \tag{12a}$$

$$\frac{\partial \bar{\rho}\tilde{u}_i}{\partial x_i} = -\frac{\partial \bar{\rho}}{\partial t}, \tag{12b}$$

$$\frac{\partial \bar{\rho}\tilde{Z}}{\partial t} + \frac{\partial}{\partial x_j}\bar{\rho}\tilde{Z}\tilde{u}_j = \frac{\partial}{\partial x_i}\left(\bar{\rho}\tilde{\alpha}\frac{\partial \tilde{Z}}{\partial x_i}\right) + \frac{\partial q_j^Z}{\partial x_j}, \tag{12c}$$

$$\frac{\partial \bar{\rho}\tilde{C}}{\partial t} + \frac{\partial}{\partial x_j}\bar{\rho}\tilde{C}\tilde{u}_j = \frac{\partial}{\partial x_i}\left(\bar{\rho}\tilde{\alpha}\frac{\partial \tilde{C}}{\partial x_i}\right) + \bar{\rho}\tilde{w}_C + \frac{\partial q_j^C}{\partial x_j}. \tag{12d}$$

Here, τ_{ij} denotes the subgrid stress and is modeled as

$$\tau_{ij} = \bar{\rho}(\widetilde{u_i u_j} - \tilde{u}_i\tilde{u}_j) = 2\mu_t \tilde{S}_{ij} - \tfrac{1}{3}\bar{\rho}q^2\delta_{ij}, \quad \mu_t = C_\mu \bar{\rho}\Delta^2\sqrt{\widetilde{S_{ij}}\,\widetilde{S_{ij}}} \tag{13}$$

and the isotropic part of the subgrid stress (q^2) is absorbed into the pressure. q_j^Z denotes the subgrid flux of the mixture fraction and is modeled as

$$q_j^Z = \bar{\rho}(\widetilde{u_j Z} - \tilde{u}_j\tilde{Z}) = \bar{\rho}\alpha_t^Z\frac{\partial \tilde{Z}}{\partial x_j}, \quad \bar{\rho}\alpha_t^Z = C_\alpha^Z\bar{\rho}\Delta^2\sqrt{\widetilde{S_{ij}}\,\widetilde{S_{ij}}}. \tag{14}$$

q_j^C denotes the subgrid flux of the progress variable which is modeled similar to the mixture fraction. The coefficients C_μ and C_α^Z are obtained using the dynamic procedure [25]. Note that the dynamic procedure makes C_α^Z dependent on the resolved velocities and mixture fraction, which introduces a dependence on mixture fraction into α_t^Z. The same holds for the progress variable diffusivity, α_t^C.

The flamelet library, i.e., Eq. (6) is highly nonlinear; the filtered variables ($\bar{\rho}$, $\tilde{T}$, $\tilde{y}_k$, and $\tilde{w}_C$), therefore, cannot be represented solely in terms of the primitive variables ($\tilde{Z}, \tilde{C}$). The probability density function (PDF) approach is used to obtain the filtered density and chemical source terms. Filtered combustion variables are obtained by integrating Eq. (6) over the joint PDF of the subgrid fluctuations in Z and λ. The presumed PDF approach is used; e.g.,

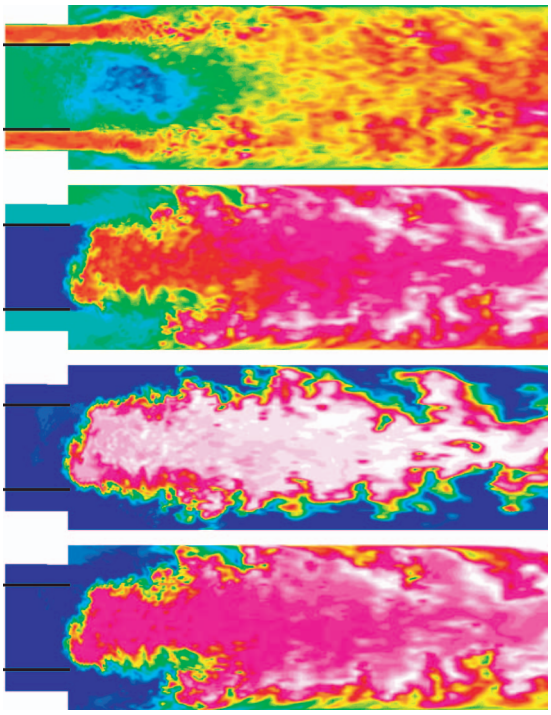

Fig. 3 Instantaneous contours of the (*a*) streamwise velocity, (*b*) temperature, (*c*) CO mass fraction, and (*d*) progress variable ($Y_{CO_2} + Y_{H_2O}$) in an azimuthal plane from LES of reacting flow in a coaxial combustor geometry

$$\bar{\rho}^{-1} = \int \rho^{-1}(Z,\lambda)\tilde{P}(Z,\lambda)dZd\lambda \quad \tilde{w}_C = \int w_C(Z,\lambda)\tilde{P}(Z,\lambda)dZd\lambda \tag{15}$$

where it is assumed that the joint PDF, $\tilde{P}(Z,\lambda) = \tilde{P}(Z)\tilde{P}(\lambda)$. Here, $\tilde{P}(Z)$ is modeled as a two-parameter beta distribution, and $\tilde{P}(\lambda)$ is modeled as a delta function [2]. Each subgrid state is, therefore, represented by a single flamelet. The assumed PDF's yield the chemical variables in terms of $\tilde{Z}$, $\widetilde{Z''^2}$, and $\tilde{\lambda}$. Note that the progress variable, $\tilde{C}$ satisfies an unsteady governing equation, (Eq. (12*d*)) in addition to being expressed in terms of Z and λ in the flamelet library. The solution procedure is to advance $\tilde{Z}$ and $\tilde{C}$ using Eqs. (12*c*) and (12*d*), and obtain $\tilde{\lambda}$ from the flamelet library. Once $\tilde{\lambda}$ is known, all other variables can be obtained, i.e., filtered values of y_k, T, ρ, w_k, μ, and α are each expressible as $f(\tilde{Z}, \widetilde{Z''^2}, \tilde{C})$. The subgrid mixture fraction variance $\widetilde{Z''^2}$ is obtained following [2];

$$\bar{\rho}\widetilde{Z''^2} = C_Z\bar{\rho}\Delta^2|\nabla\tilde{Z}|^2, \tag{16}$$

where the coefficient C_Z is calculated dynamically.

3.4 Reacting Flow Simulations in a Coaxial Combustor Geometry. LES was performed for a methane fueled, coaxial combustor under conditions corresponding to experiments by Spadaccini et al. [30]. Results from a previous calculation using a structured code by Pierce and Moin [2], and experimental data of Spadaccini et al. [30] were used for validation. The quantities validated include mean velocity profiles, temperature and chemical species at several stations inside the combustion chamber. A cross section of the axisymmetric geometry is seen in Fig. 3. Fuel was introduced through the circular core section at a relatively low velocity of 0.93 m/s, and nonswirling air was introduced through the surrounding annulus at a much higher mean velocity

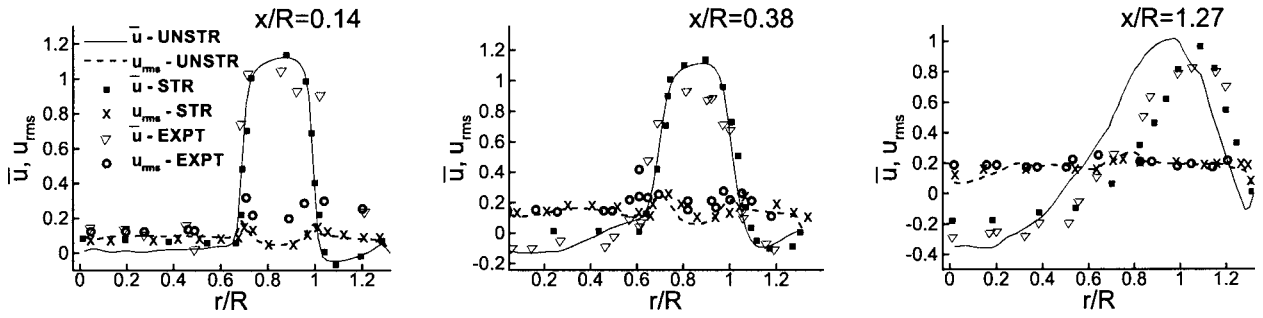

Fig. 4 Comparison of the mean and rms values of the streamwise velocity in unstructured grid LES (UNSTR) to Spadaccini et al. [30] experiments (EXPT) and Pierce and Moin's [2] LES on structured grids (STR)

of $U=20.6$ m/s. The mass flow rates of the fuel and air in the inlet sections were 0.0072 and 0.137 kg/s, respectively, the air temperature was 750 K, and the fuel temperature was 300 K. The mean pressure in the combustor was 3.8 atm. The fuel used in the experiment was natural gas but was assumed to be pure methane in the computations; Pierce and Moin [2] make the same assumption. The exterior radius of the annulus was $R=4.865$ cm, and is used for nondimensionalization. The Reynolds number of the air stream was 50,000 at the inflow.

A computational grid containing approximately 1.3 million hexahedral elements was used. The grid resolution in the region where the fuel and air streams mix, was comparable to that in Pierce and Moin's structured grid simulations which use approximately 2.5 million elements. The main combustor chamber was $12R$ long, and the computational inflow plane extended $1R$ upstream. Fully developed turbulent inflow conditions from separate calculations for a periodic pipe and annular pipe domains were specified at the inflow. The mixture fraction at the inflow, was unity for the fuel stream, and zero for the air stream. The progress variable, C was zero at the inflow for both streams. Fully developed incompressible velocity and scalar fields were obtained before the chemistry model was turned on. The initial progress variable scalar field was set to its maximum allowed value determined from fast chemistry, so that initially the flame was fully ignited. A chemical table corresponding to methane and the specified combustor pressure was precalculated (Pierce, private communication). The product mass fraction was chosen as the progress variable.

Figure 3 show instantaneous contours of the velocity, temperature, mixture fraction, and progress variable, respectively. Because of the high air/fuel velocity ratio, a strong central recirculation region is formed in front of the fuel port. The recirculating combustion products provide a continuous ignition source for the relatively cold incoming reactants, thereby stabilizing the flame. Note that mixture fraction is computed based on the total carbon and hydrogen atoms mass fractions, and the product mass fraction is computed from $y_{CO_2}+y_{H_2O}$. In the experiment, the flame location was observed to lift off the burner and reattach intermittently in a highly unsteady asymmetric manner. The LES also predicts a lifted flame; animation of the progress variable contours shows similar unsteady behavior of the flame front. Figures 4–8 compare statistics of the mean and fluctuating streamwise velocity, temperature, mixture fraction, progress variable, and CO mass fraction to experiment, and Pierce and Moin's [2]) structured grid

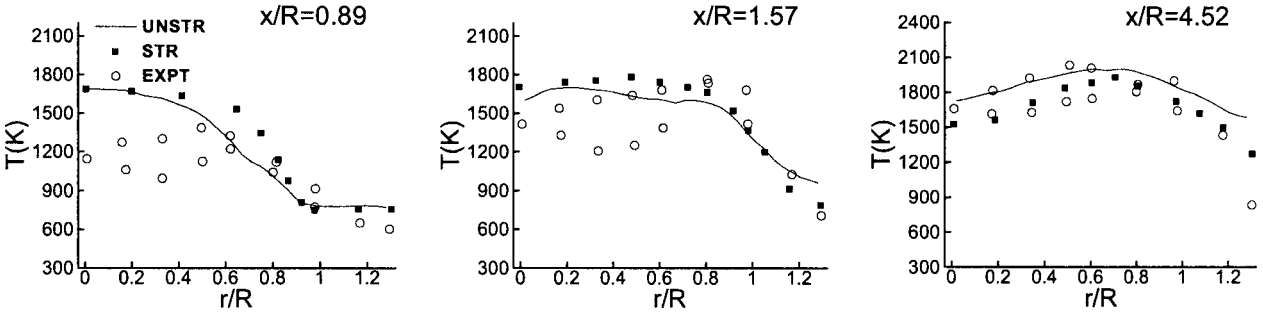

Fig. 5 Comparison of the mean temperature in unstructured grid LES (UNSTR) to Spadaccini et al. [30] experiments (EXPT) and Pierce and Moin's [2] LES on structured grids (STR)

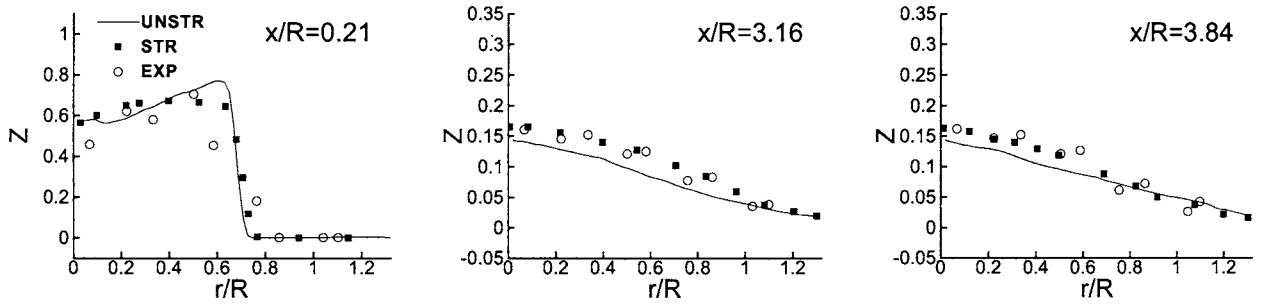

Fig. 6 Comparison of the mixture fraction in unstructured grid LES (UNSTR) to Spadaccini et al. [30] experiments (EXPT) and Pierce and Moin's [2] LES on structured grids (STR)

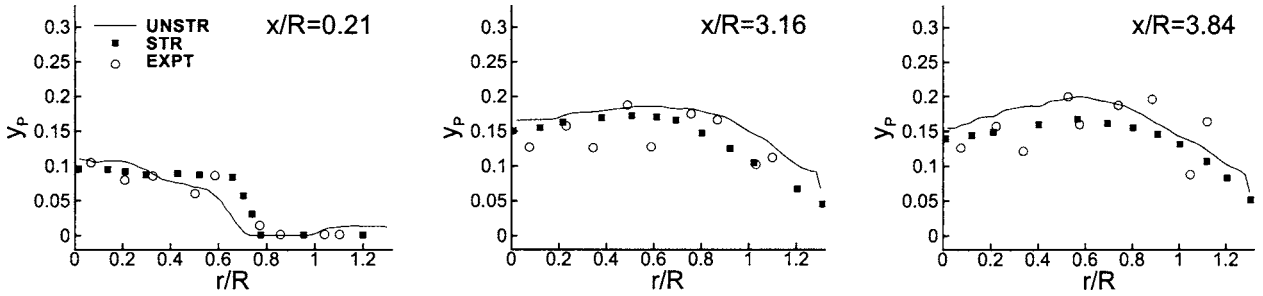

Fig. 7 Comparison of progress variable ($Y_{CO_2}+Y_{H_2O}$) between unstructured grid LES (UNSTR) to Spadaccini et al. [30] experiments (EXPT) and Pierce and Moin's [2] structured grid LES (STR)

computations, and acceptable agreement is found.

Note that the purpose of comparison to Pierce and Moin's [2] computations is validation; it is not intended to suggest that the unstructured approach is superior to a structured grid approach for the coaxial combustor geometry. In fact, for simple configurations like the coaxial combustor, a structured grid solver would be more efficient. However, an unstructured grid methodology affords more generality, and is easily applied to significantly more complex geometries like the commercial gas-turbine combustor discussed below.

3.5 Reacting Flow in Gas Turbine Combustor Geometry. LES of turbulent reacting flow was performed in the combustor geometry of a Pratt and Whitney gas-turbine engine. The simulation is performed for the sector corresponding to one of 18 injectors. Figure 9 shows the level of geometrical complexity; the combustor has numerous passages, holes of various sizes and shapes, swirlers, and obstacles in the flow path. The combustor chamber is fed by three coaxial swirlers and several dilution holes. The inlet air passes through the pre-diffuser and follows two paths; the main stream flows through the swirlers and enters the chamber,

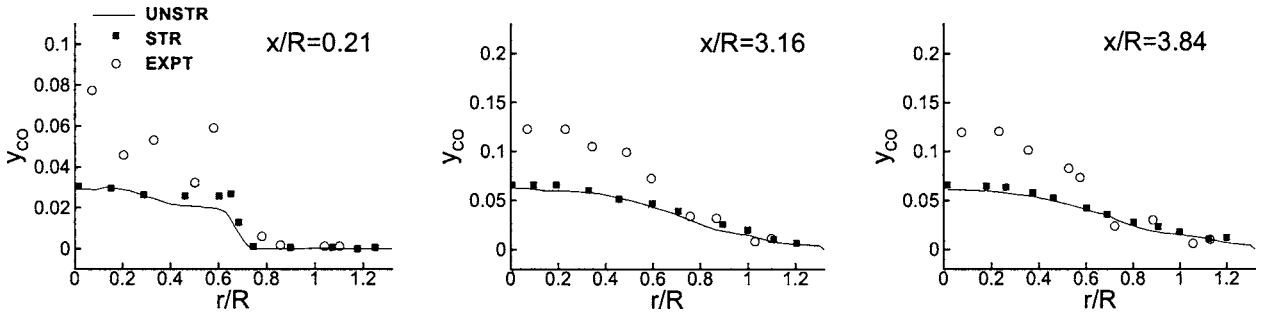

Fig. 8 Comparison of CO mass fraction between unstructured grid LES (UNSTR) to Spadaccini et al. [30] experiments (EXPT) and Pierce and Moin's [2] structured grid LES (STR)

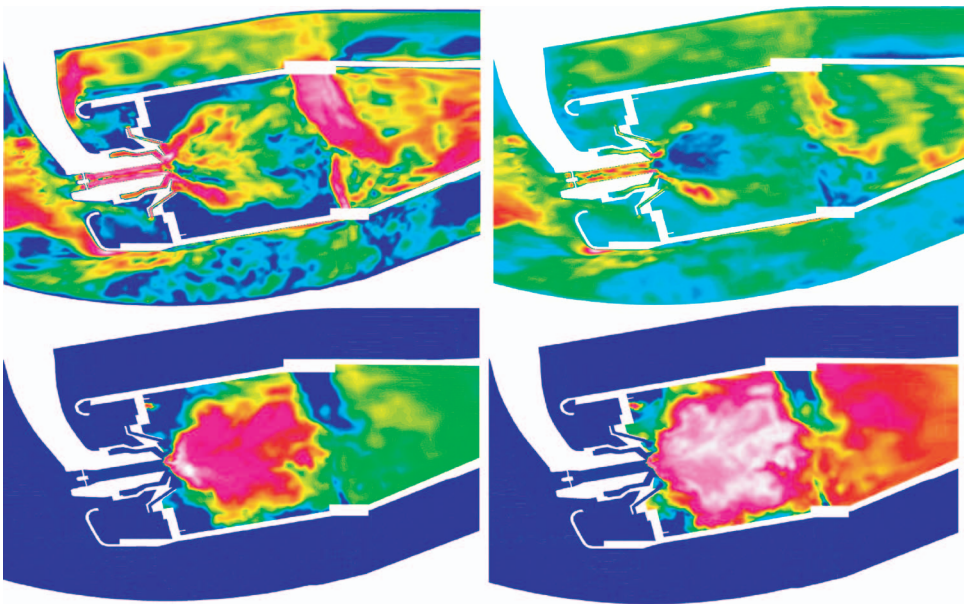

Fig. 9 Instantaneous contours of the (*a*) velocity magnitude, (*b*) streamwise velocity, (*c*) mixture fraction, and (*d*) progress variable from LES of reacting flow in gas turbine combustor geometry

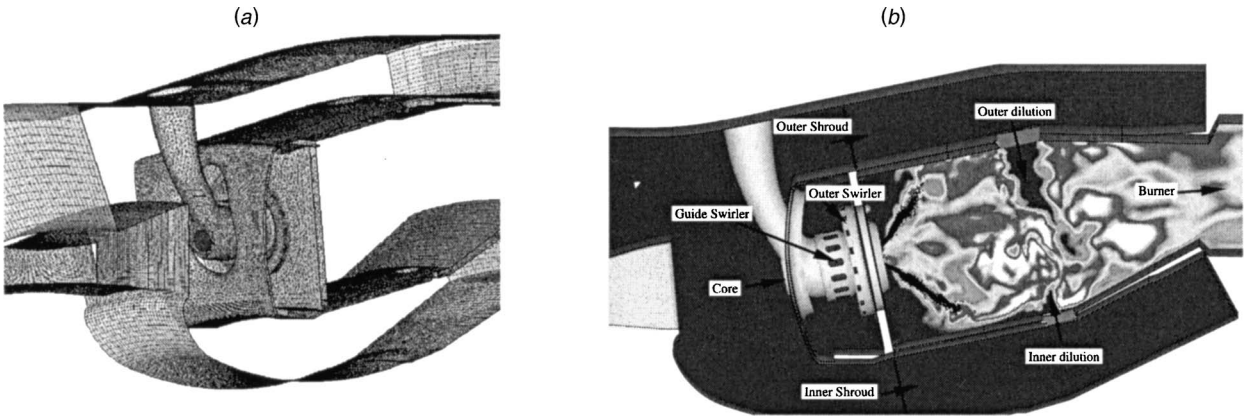

Fig. 10 (*a*) Gas turbine combustor sector geometry. (*b*) Instantaneous position of fuel spray superposed on contours of temperature from LES of reacting flow in gas turbine combustor geometry.

while the secondary stream is diverted to the outer diffusers, and enters the combustor through the dilution holes. The computations include the effects of flow bleed and transpiration, whose values are specified as boundary conditions.

The Reynolds number based on radial height, and mean velocity in the inlet section of the pre-diffuser is around 600,000. The Reynolds number inside the core swirler channel is about 150,000. The fuel was Jet A; a corresponding flamelet library for the two-component surrogate (80% *n*-decane and 20% 1,2,4-rrimethyl-benzene) was generated. This chemical mechanism contains approximately 1000 elementary reactions among 100 chemical species (Pitsch, private communication).

The algorithm and subgrid model described in Sec. 3 were used to perform the simulations. In addition, a Lagrangian approach was used to model the fuel as a spray, which atomizes, breaks up, and evaporates. The inter-phase mass, momentum and energy transfer is modeled using two-way coupling. Two-way coupling between the gas- and liquid phases was accounted for. Details of the Lagrangian extension to the gas-phase algorithm are described by Refs. [1,28,29]; only the results are shown here. Liquid fuel is specified as a boundary condition over a thin ring at the injector exit. Also, flow rates corresponding to outflow from the outer diffuser to the secondary cooling systems, and transpiration through the combustor liners are specified as boundary conditions from experiment.

A hybrid unstructured grid of approximately 1.9 million elements (hexahedral, tetrahedral, and pyramids) was used to perform the simulations. The cold-flow simulations were used to initialize a gas-phase reacting flow. The mass-flow rate of the gas phase in the fuel inlet sections were matched to their experimental value. After a statistically stationary gas-phase flow was obtained, fuel was then re-specified as liquid. The liquid fuel emerges as a conical spray, which breaks up and evaporates downstream of the injector. Figure 10 shows a snapshot of the region immediately downstream of the injector, where particle positions corresponding to the spray droplets are superposed on contours of velocity magnitude. Contours of the velocity magnitude, axial velocity, mixture fraction, and progress variable are shown in Fig. 9. The correspondence between the progress variable and temperature is apparent. Swirl is seen to set up a recirculating region downstream of the injector. The fuel and air streams diverge radially; their interaction produces a lifted flame and an associated increase in temperature. In contrast to cold flow [1], heat release accelerates the fluid axially. This acceleration is evident in the dilution hole jets displaying a shallower trajectory as compared to the cold flow. The hot combustion products, and recirculation prevent flame blow out. Cold dilution jets interact with the combustion products to noticeably decrease the temperature. Proprietary experimental data for the mass splits were used for validation. The error between LES and experiment is shown in Table 1, and seen to be quite acceptable.

Table 1 Comparison of mass splits between simulation and experiment in gas turbine combustor geometry. The absolute value of the percentage error computed with respect to the experimental value is shown. Figure 10(*b*) defines the various flow passages in the table.

Location	LES error (%)
Outer dilution hole	5.85
Inner dilution hole	0.20
Outer shroud	3.83
Inner shroud	0.47
Core swirler	2.9
Outer swirler	0.86
Guide swirler	1.36
Burner	0.26

Acknowledgment

This work was supported by the United States Department of Energy under the Accelerated Strategic Computing Initiative. Computing resources provided by the San Diego Supercomputing Center, Lawrence Livermore National Laboratory, and the Minnesota Supercomputing Institute are gratefully acknowledged. We are grateful to Dr. Heinz Pitsch for useful technical discussions, and Dr. Saadat Syed at Pratt and Whitney for providing proprietary experimental data, the combustor geometry, and valuable technical input.

References

[1] Mahesh, K., Constantinescu, G., and Moin, P., 2004, "A Numerical Method for Large Eddy Simulations in Complex Geometries," J. Comput. Phys., **197**, pp. 215–240.
[2] Pierce, C., and Moin, P., 2004, "Progress-Variable Approach for Large-Eddy Simulation of Nonpremixed Turbulent Combustion," J. Fluid Mech., **504**, pp. 73–97.
[3] Kim, W.-W., and Syed, S., 2004, "Large-Eddy Simulation Needs for Gas-Turbine Combustor Design," AIAA Paper No. 2004-0331.
[4] Mongia, H. C., 2003, "Recent Advances in the Development of Combustor Design Tools," AIAA Paper No. 2003–4495.
[5] Menon, S., 2003, "Modeling Pollutant Emission and Lean Blow Out in Gas Turbine Combustors," AIAA Paper No. 2003–4496.
[6] Mari, C., and Mahias, O., 2003, "Numerical Modeling at SNECMA: Current Status and Outlooks for the Future," ISABE Paper No. 2003-1005.
[7] Peters, N., 2000, *Turbulent Combustion*, Cambridge University Press, Cambridge, UK.
[8] Peters, N., 1984, "Laminar Diffusion Flamelet Models in Nonpremixed Turbulent Combustion," Prog. Energy Combust. Sci., **10**, pp. 319–339.
[9] Klimenko, A. Yu., and Bilger, R. W., 1999, "Conditional Moment Closure for Turbulent Combustion," Prog. Energy Combust. Sci., **25**, pp. 595–687.
[10] Pope, S. B., 1985, "PDF Methods for Turbulent Reactive Flows," Prog. Energy

Combust. Sci., **11**, pp. 119–192.
[11] Kerstein, A. R., 1992, "Linear Eddy Modeling of Turbulent Transport. Part 7 Finite Rate Chemistry and Multi-Stream Mixing," J. Fluid Mech., **240**, pp. 289–313.
[12] McMurtry, P. A., Menon, S., and Kerstein, A. R., 1993, "Linear Eddy Modeling of Turbulent Combustion," Energy Fuels, **7**, pp. 817–826.
[13] Calhoon, W. H., and Menon, S., 1996, "Subgrid Modeling for Reacting Large-Eddy Simulations," AIAA Paper No. 96–0516.
[14] Cook, A. W., Riley, J. J., and Kosaly, G., 1997, "A Laminar Flamelet Approach to Subgrid-Scale Chemistry in Turbulent Flows," Combust. Flame, **109**, pp. 332–341.
[15] Reveillon, J., and Vervisch, L., 1996, "Subgrid-Scale Turbulent Micromixing: Dynamic Approach," AIAA J., **36**, pp. 336–341.
[16] Colucci, P. J., Jaberi, F. A., Givi, P., and Pope, S. B., 1998, "Filtered Density Function for Large-Eddy Simulation of Turbulent Reacting Flows," Phys. Fluids, **10**, pp. 499–515.
[17] Legier, J. P., Poinsot, T., and Veynante, D., 2000, "Dynamically Thickened Flame LES Model for Premixed and Nonpremixed Turbulent Combustion," *Proceedings 2000 Summer Program*, Center for Turbulence Research, NASA-Ames/Stanford University, pp. 157–168.
[18] Pitsch, H., and Steiner, H., 2000, "Large-Eddy Simulation of a Turbulent Piloted Methane/Air Diffusion Flame (Sandia Flame D)," Phys. Fluids, **12**, pp. 2541–2554.
[19] Steiner, H., and Bushe, W. K., 2001, "Large-Eddy Simulation of a Turbulent Reacting Jet With Conditional Source Term Estimation," Phys. Fluids, **13**, pp. 754–769.
[20] Mittal, R., and Moin, P., 1997, "Suitability of Upwind Biased Schemes for Large-Eddy Simulation," AIAA J., **30**(8), pp. 1415–1417.
[21] Arakawa, A., 1966, "Computational Design for Long Term Numerical Integration of the Equations of Fluid Motion: Two-dimensional Incompressible Flow, Part I," J. Comput. Phys., **1**, pp. 119–143.
[22] Fromm, J. E., and Harlow, F. H., 1963, "Numerical Solution of the Problem of Vortex Street Development," Phys. Fluids, **6**, pp. 175–182.
[23] Lilly, D. K., 1965, "On the Computational Stability of Numerical Solutions of Time-Dependent Nonlinear Geophysical Fluid Dynamics Problems," Mon. Weather Rev., **93**, pp. 11–26.
[24] Mansour, N. N., Moin, P., Reynolds, W. C., and Ferziger, J. H., 1979, "Improved Methods for Large-Eddy Simulation of Turbulence," *Proc. Turbulent Shear Flows I*, F. Durst, B. E. Launder, F. W. Schmidt, and J. H. Whitelaw, eds. Springer-Verlag, Berlin, pp. 386–401.
[25] Germano, M., Piomelli, U., Moin, P., and Cabot, W. H., 1991, "A Dynamic Subgrid-Scale Eddy Viscosity Model," Phys. Fluids A, **3**(7), pp. 1760–1765.
[26] Lilly, D. K., 1992, "A Proposed Modification of the Germano Subgrid-Scale Closure Method," Phys. Fluids A, **4**(3), pp. 633–635.
[27] Sommerfeld, M., and Qiu, H. H., 1991 "Detailed Measurements in a Swirling Particulate Two-Phase Flow by a Phase-Doppler Anemometer," Int. J. Heat Fluid Flow, **12**(1), pp. 20–28.
[28] Apte, S. V., Mahesh, K., Moin, P., and Oefelein, J. C., 2003a, "Large-Eddy Simulation of Swirling Particle-Laden Flow in a Coaxial-Jet Combustor," Int. J. Multiphase Flow, **29**(8), pp. 1311–1331.
[29] Apte, S. V., Mahesh, K., Ham, F., Constantinescu, G., and Moin, P., 2003b, "Large-Eddy Simulation of Multiphase Flows in Complex Combustors," *Computational Methods in Multiphase Flow II*, A. A. Mammoli and C. A. Brebbia, eds. WIT, UK, pp. 53–62.
[30] Spadaccini, L. J., Owen, F. K., and Bowman, C. T., 1976, "Influence of Aerodynamic Phenomena on Pollutant Formation in Combustion (Phase I. Gaseous fuels)," U.S. Environmental Protection Agency Report No. EPA-600/2-76-247a.